JWST Observations of the Ring Nebula (NGC 6720). III. A Dusty Disk around Its Central Star

Raghvendra Sahai[1], Griet Van de Steene[2], Peter A. M. van Hoof[2], Albert Zijlstra[3], Kevin Volk[4], Harriet L. Dinerstein[5], Michael J. Barlow[6], Els Peeters[7,8,9], Arturo Manchado[10,11,12], Mikako Matsuura[13], Jan Cami[7,8,9], Nick L. J. Cox[14,15], Isabel Aleman[16], Jeronimo Bernard-Salas[14,15], Nicholas Clark[7], Kay Justtanont[17], Kyle F. Kaplan[5], Patrick J. Kavanagh[18], and Roger Wesson[6,13]

[1] Jet Propulsion Laboratory, California Institute of Technology, Pasadena, CA 91109, USA
[2] Royal Observatory of Belgium, Ringlaan 3, B-1180 Brussels, Belgium
[3] Jodrell Bank Centre for Astrophysics, Department of Physics & Astronomy, The University of Manchester, Oxford Road, Manchester M13 9PL, UK
[4] Space Telescope Science Institute, 3700 San Martin Drive, Baltimore, MD 21218, USA
[5] University of Texas at Austin, Austin, TX 78712, USA
[6] Department of Physics and Astronomy, University College London, Gower Street, London WC1E 6BT, UK
[7] Department of Physics and Astronomy, University of Western Ontario, London, Ontario, ON N6A 3K7, Canada
[8] Institute for Earth and Space Exploration, University of Western Ontario, London, Ontario, ON N6A 3K7, Canada
[9] SETI Institute, 189 Bernardo Avenue, Suite 100, Mountain View, CA 94043, USA
[10] Instituto de Astrofísica de Canarias, 38200 La Laguna, Tenerife, Spain
[11] Universidad de La Laguna (ULL), Astrophysics Department, 38200 La Laguna, Tenerife, Spain
[12] CSIC, Av. Astrofísico Francisco Sánchez, 3, 38206 La Laguna, Tenerife, Spain
[13] Cardiff Hub for Astrophysics Research and Technology (CHART), School of Physics and Astronomy, Cardiff University, The Parade, Cardiff CF24 3AA, UK
[14] ACRI-ST, Centre d'Etudes et de Recherche de Grasse (CERGA), 10 Av. Nicolas Copernic, 06130 Grasse, France
[15] INCLASS Common Laboratory, 10 Av. Nicolas Copernic, 06130 Grasse, France
[16] Laboratório Nacional de Astrofísica, Rua dos Estados Unidos, 154, Bairro das Nações, Itajubá, MG, CEP 37504-365, Brazil
[17] Chalmers University of Technology, Department of Space, Earth and Environment, Onsala Space Observatory, S-439 92 Onsala, Sweden
[18] Department of Experimental Physics, Maynooth University, Maynooth, Co Kildare, Ireland

Abstract

The planetary nebula NGC 6720, also known as the "Ring Nebula," is one of the most iconic examples of nearby planetary nebulae whose morphologies present a challenge to our theoretical understanding of the processes that govern the deaths of most stars in the Universe that evolve on a Hubble time. We present new imaging with JWST of the central star of this planetary nebula (CSPN) and its close vicinity, in the near-to-mid-IR wavelength range. We find the presence of a dust cloud around the CSPN, both from the spectral energy distribution at wavelengths $\gtrsim 5\,\mu$m as well as from radially extended emission in the 7.7, 10, and 11.3 μm images. From the modeling of these data, we infer that the CSPN has a luminosity of $310\,L_\odot$ and is surrounded by a dust cloud with a size of ~ 2600 au, consisting of relatively small amorphous silicate dust grains (radius $\sim 0.01\,\mu$m) with a total mass of $1.9 \times 10^{-6}\,M_\oplus$. However, our best-fit model shows a significant lack of extended emission at 7.7 μm—we show that such emission can arise from a smaller ($7.3 \times 10^{-7}\,M_\oplus$) but uncertain mass of (stochastically heated) ionized polycyclic aromatic hydrocarbon (PAHs). However, the same energetic radiation also rapidly destroys PAH molecules, suggesting that these are most likely being continuously replenished, via the outgassing of cometary bodies and/or the collisional grinding of planetesimals. We also find significant photometric variability of the central source that could be due to the presence of a close dwarf companion of mass $\leqslant 0.1\,M_\odot$.

Unified Astronomy Thesaurus concepts: Planetary nebulae (1249); Stellar mass loss (1613); Post-asymptotic giant branch (1287); Circumstellar dust (236); James Webb Space Telescope (2291); Silicate grains (1456); Polycyclic aromatic hydrocarbons (1280); Infrared astronomy (786); Planetesimals (1259); Ultraviolet spectroscopy (2284); Gaia (2360); Light curves (918)

1. Introduction

The presence and origin of dusty disks around main-sequence (MS) and pre-MS stars are well understood. These are first seen as the gas-and-dust-rich planet-forming disks in young stellar objects, and are an integral part of the star formation process itself, and are then seen as the gas-poor debris disks around MS stars resulting from the collisions of large planetesimals that produce second-generation dust particles (G. H. Rieke et al. 2005). The dust in these debris disks dissipates long before the stars evolve off the MS.

Remarkably, dusty disks or disk-like structures manifest themselves again as these stars reach the ends of their lives as asymptotic giant branch (AGB) stars, post-AGB stars, and the central stars of planetary nebulae (PNs; e.g., R. Sahai et al. 2007, 2011; M. Hillen et al. 2017). AGB stars, representing the death throes of stars with MS masses of ~ 1–$8\,M_\odot$, are very luminous ($L \sim 5000$–$10{,}000\,L_\odot$) and cool ($T_{\rm eff} < 3000\,$K) and experience heavy mass loss (with rates up to $10^{-4}\,M_\odot\,{\rm yr}^{-1}$; see, e.g., the review by L. Decin 2021) that depletes most of the stellar envelope and accelerates their evolution to the PN phase, through a transitory post-AGB phase. These stars evolve to higher temperatures through the post-AGB and PN phases at almost constant luminosity, fading and becoming white dwarfs (WDs) at the ends of their lives. It is during these post-AGB and WD phases that the presence of disk-like structures around
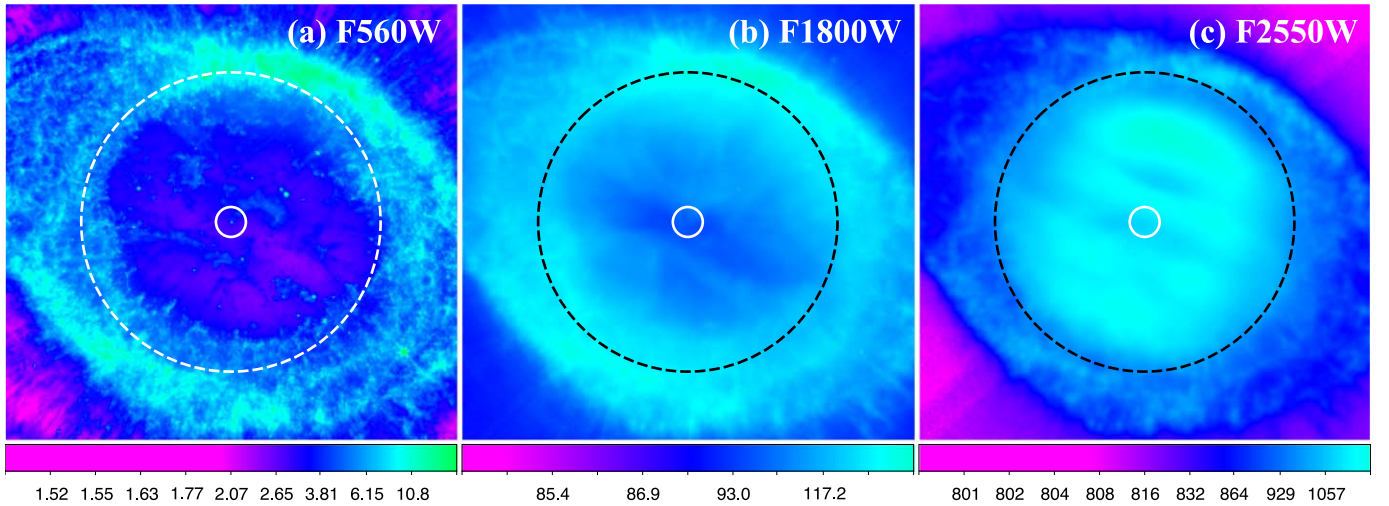
Figure 1. JWST/MIRI images showing the extended nebular emission around NGC 6720's CS in three filters: (a) F560W; (b) F1800W; and (c) F2550W. The large dashed circles (of radius 25″) in each panel show an extended nebular region around the CS (located at the center of the small circle or radius 2″.5). Intensity units (MJy sr^{-1}) are shown in the scale bars at the bottom of each image.

the central stars becomes observationally apparent once again, raising questions about their nature, formation, longevity, and potentially a second phase of planet formation. The disks have a large range of sizes, found from direct imaging or derived from modeling the spectral energy distribution (SED). These disks range from very small disks found around cool central WD stars ($\lesssim$0.01 au; e.g., N. P. Ballering et al. 2022) to much larger disks extending to radii up to ∼1000 au that have been found in AGB stars (e.g., R. Sahai et al. 2022), post-AGB stars (e.g., S. de Ruyter et al. 2006), and the central stars of PNs (e.g., K. Y. L. Su et al. 2007; Y.-H. Chu et al. 2011; J. Bilíková et al. 2012; R. Sahai et al. 2023).

We report here new JWST observations of the central star (and its immediate environment) of the iconic PN the Ring Nebula (NGC 6720), resulting in the discovery of the second resolved dusty disk around a CSPN.[19] We will hereafter refer to the central star (i.e., the WD) as the CSPN; the CSPN and its immediate environment will be referred to as the central source or CS. This PN, of long-standing interest for both amateur and professional astronomy, has been extensively studied, both from ground-based (e.g., B. Balick et al. 1992; M. Bryce et al. 1994; M. A. Guerrero et al. 1997) and space-based observatories (R. Sahai et al. 2012; C. R. O'Dell et al. 2013), yet it continues to be an amazing astrophysical laboratory, yielding new and unexpected insights into the extraordinary deaths of intermediate-mass stars (e.g., R. Wesson et al. 2024; J. H. Kastner et al. 2025). NGC 6720 was imaged through a wide suite of filters from 1.6 to 25 μm using the NIRCAM and MIRI instruments on JWST via program ID GO-01558 (R. Wesson et al. 2024). A log of the observations is provided in Table 1 of R. Wesson et al. (2024), who carried out an imaging study of rings, globules, and arcs in the nebula. R. Wesson et al. (2024) found that NGC 6720's CSPN has two companions. One of these is a distant mid-K-spectral-type dwarf companion, CSPN(B), based on its having the same parallax and proper motion as NGC 6720's CSPN, CSPN(A) (I. Gonzalez-Santamaria et al. 2021), with a projected separation of ∼15,000 au. In addition, there is another possible

companion, CSPN(C), which is much closer, with a period of about 280 ± 70 yr, and thus at a separation of 50 ± 15 au, inferred from the presence of low-contrast, regularly spaced concentric arc-like features seen in the F770W, F100W, and F1130W images of the nebula. The R. Wesson et al. (2024) study is the first publication of several studies of this object using data from JWST program GO-01558, including this paper and two studies of key diagnostic regions of the nebula, one focusing on the polycyclic aromatic hydrocarbon (PAH) emission (N. Clark et al. 2025) and another on the rich H$_2$ emission-line spectrum (P. A. M. van Hoof et al. 2025, in preparation).

The paper is organized as follows. In Section 2, we describe the imaging observations of the CS of NGC 6720; in Section 2.1, we describe the construction of the full SED of the CS from UV-to-IR wavelengths as well as the characterization of the extended mid-IR emission; in Section 3, we derive the properties of the CSPN from fitting the UV-to-near-IR SED; in Section 4, we model the dust emission; in Section 5, we discuss the optical photometric variability of the CS; in Section 6, we discuss the implications of our results for the origin and formation of the NGC 6720 CS disk, including the possible presence and role of unseen bound companions; and in Section 7, we summarize the main conclusions of our study.

2. The Central Star of NGC 6720 and Its Near Environment

The extended morphology of the nebula from 2 to 21 μm shows that the CS is located within a roughly circular region of radius about 25″ that is of relatively low surface brightness in the NIRCAM images, as well as the MIRI images in most of the filters (F560W, F770W, F1130W, F1280W, F1500W, and F2100W; Figure 1; see also Figures 1, 4, and 5 of R. Wesson et al. 2024). The exceptions are the F1000W, F1800W, and F2550W filters, in which the central region is almost filled, and almost as bright (F1800W) or brighter than the main ring (F1000W and F2550W), except for a roughly linear structure that is relatively "dark" and lies approximately along the major axis of the nebula (Figure 1). The F1000W filter includes strong gas emission lines of [S IV] and [Ar III] in its bandpass; the F1800W filter includes a strong contribution from [S III].

---

[19] The first being the dusty disk around the CSPN of the Southern Ring, NGC 3132 (R. Sahai et al. 2023).
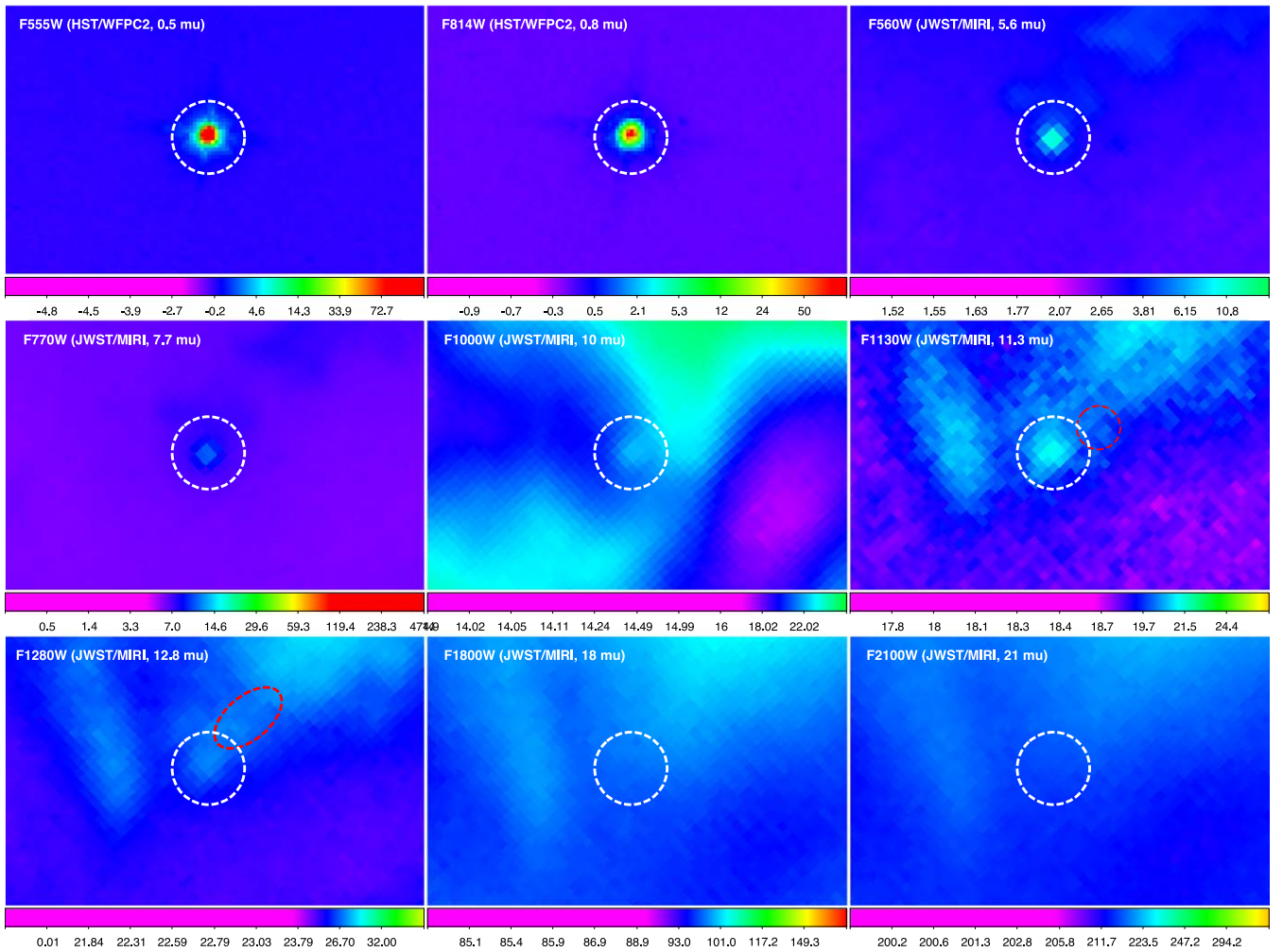
Figure 2. Comparison of JWST/MIRI images of the central region of NGC 6720, taken in seven filters covering the 5.6–21 μm wavelength range (F560W, F770W, F1000W, F1130W, F1280W, F1800W, and F2100W), with Hubble Space Telescope/ WFPC2 images at optical wavelengths (0.55 μm—F555W and 0.81 μm—F814W). The white dashed circles (of diameter 1″) locate the central WD star in the images. Intensity units are shown in the scale bars at the bottom of each image: counts s^{-1} (cps) per pixel for the Hubble Space Telescope images (1 cps per pixel is 8.32 MJy sr^{-1} and 12.9 MJy sr^{-1}, respectively, in the F555W and F814W images) and MJy sr^{-1} for the JWST images. The red ellipse in the F1280W image shows the location of an elongated nebular feature, "spur(nw)," which lies close to and/or overlaps the CS. The red circle in the F1130W image shows a region of nebular emission in the near vicinity of the CS used for comparing the mid-IR colors of the nebular emission with those of the CS.

The F2550W filter includes the strong [O IV] line. The CS (Figure 2) is located within the linear structure and is generally well isolated from surrounding nebulosity in filters with central wavelengths shortward and including 7.7 μm, but it lies on the edge of bright nebular[20] emission in the images at longer wavelengths. No localized emission on the CSPN can be seen in filters with central wavelengths longward of 12.8 μm.

2.1. SED and Radial Intensities

We have constructed the SED of the CS over the UV-to-mid-IR ($\sim$0.09–21 μm) range as follows. The SED in the optical–UV–near-IR range was determined using archival UV spectra from IUE[21] and published optical–near-IR photometry (Table 1). For the near-to-mid-IR region, we used the JWST imaging data from NIRCAM and MIRI. We extracted photometry of the CS from the NIRCAM images obtained

with the filters F162M, F212N, F300M, and F335M, using relatively small circular apertures for the CS and annular apertures for the sky background (Table 1), with aperture corrections determined using field stars (Table 2), as described by R. Sahai et al. (2023) for the CS of the PN NGC 3132.

A different strategy was adopted for the MIRI images, which show the presence of underlying and/or nebular structures in the near vicinity of the CS. Images with the filters F560W, F770W, F1000W, and F1130W show a clear local brightness peak centered on the CS. For these, we: (i) subsampled each image by a factor of 3; and (ii) extracted a radial intensity distribution, I(r), for each filter, by averaging the intensity over an angular wedge, with its vertex centered on the CS and a specific angular range chosen to avoid the nebular contamination in the vicinity.

In all filters shortward of and including F560W, the CS appears to be point-like (Figures 2 and 3). The radial intensity cuts for the F770W, F1000W, and F1130W images show a CS with an FWHM comparable to (or slightly larger than) that of the corresponding point-spread function (PSF), together with a weaker "skirt" of emission at larger radii (Figure 3). These cuts

---

[20] We use the term "nebular" here and elsewhere to mean "belonging to larger structures that are part of the large PN and not localized around the CSPN."
[21] https://archive.stsci.edu/missions/iue.

Table 1
Photometry of the CS of NGC 6720

Filter	Wavelength (μm)	Flux (mJy)	Error[a] (percent)	Apert. Rad.[b] (arcsec)	Apert. Corr.[c]	Apert. PA[d] (deg)	Phot Reference[e]
B	0.43	2.80	10	...	...	...	15.405[f] (2)
V	0.555	1.79	10	...	...	...	15.769[f] (2)
G band	0.622	1.78	10	...	...	...	15.646 (3)
R	0.71	1.34	10	...	...	...	15.901[g] (1)
I	0.798	0.92	10	...	...	...	16.602[g] (1)
J	1.235	0.45	10	...	...	...	16.40[g] (1)
F162M	1.62	0.241	10	0″50	1.0	...	(4)
F212N	2.12	0.134	10	0″30	0.94	...	(4)
F300M	3.0	0.066	10	0″50	0.95	...	(4)
F335M	3.35	0.0525	10	0″50	0.94	...	(4)
F560W	5.60	0.028[h]	10	0″14	0.31	203–323	(4)
F560W	5.60	0.031[j]	10	1″8	...	203–323	(4)
F770W	7.70	0.015[h]	15	0″18	0.50	178–268	(4)
F770W	7.70	0.047[j]	15	1″8	...	178–268	(4)
F1000W	10.0	0.016[h]	30	0″23	0.50	156–180	(4)
F1000W	10.0	0.058[j]	30	1″8	...	156–180	(4)
F1130W	10.0	0.012[h]	30	0″24	0.47	156–180	(4)
F1130W	10.0	0.037[j]	30	1″8	...	156–180	(4)
F1280W	11.3	<0.010[k]	...	0″23	...	...	(4)
F1500W	15.0	<0.058[k]	...	0″28	...	...	(4)
F1800W	18.0	<0.045[k]	...	0″34	...	...	(4)
F2100W	21.0	<0.088[k]	...	0″39	...	...	(4)

Notes.
[a] Percentage error in flux of Column (3).
[b] Radius for the aperture photometry or outer radius used for integrating the radial intensity to determine the flux in filters where CS emission is extended—for the latter, no aperture correction is required.
[c] Aperture correction (for the aperture photometry) determined using field stars.
[d] Position angles defining the full angular wedge used to extract the radial intensity.
[e] References for photometry: (1) O. De Marco et al. (2013); (2) Hubble Source Catalog V.3 (B. C. Whitmore et al. 2016); (3) Gaia DR3 (Gaia Collaboration 2023); and (4) this work—when the photometry reference provides magnitudes, these are listed here.
[f] AB magnitude.
[g] Vega magnitude.
[h] Core flux, $F_{\rm core}$, derived from the integration of the radial intensity to radius $0.5 \times$ FWHM of the PSF.
[j] Flux derived from the integration of the radial intensity to the outer radius in Column (5).
[k] Upper limit for the core flux derived using the method described in Section 2.1.

Table 2
Field Stars Used for Generating PSFs and Aperture Corrections

Star	Filter	R.A. (J2000.0)	Decl. (J2000.0)
fs1	F560W	18:53:30.782	+33:01:42.70
fs3	F770W	18:53:39.842	+33:01:46.30
fs4	F1000W	18:53:40.775	+33:01:40.90
fs1	F1130W	18:53:30.782	+33:01:42.70

show that the F770W image has the weakest and least extended nebular emission near the CS, whereas the F1000W image has the strongest and most extended nebular emission near the CS. The PSF for each filter was determined from the corresponding field stars used for the aperture correction for that filter (Table 2). The F1000W image has a faint nebular structure that cuts across the selected angular wedge at a radial offset of about 1″25, resulting in a broad bump in the radial intensity. Hence, for this filter, we made a linear interpolation of the intensity across the edges of this bump (the dashed line in Figure 3(c)). For each of the filters F560W, F770W, F1000W, and F1130W, we measure a: (i) core flux, $F_{\rm core}$ ($F_{\rm tot}$), by integrating the radial intensity curve to a radius equal to $0.5 \times$ FWHM of the image PSF in that filter; and (ii) a total

flux, by integrating the radial intensity curve to a radius of 1″8, where the radial intensity is zero. The total flux is significantly lower than the total flux in all filters, except F560W, showing that the bulk of the emission at wavelengths $\sim 7.7~\mu$m and longer comes from the extended component in the CS.

For each filter, in order to assess systematic uncertainties in the radial intensity (the "full-wedge" intensity), we also extract two "half-wedge" intensities, which are the average intensities averaged over two equal contiguous halves that together span the full angular range for that filter. The differences between the full-wedge and half-wedge intensities (the red and green curves in Figure 3) show that these arise at relatively large radial offsets, where the emission is relatively low, and are therefore much more affected by uncertainties in the sky background level. The exception to this is the F1130W filter, which also shows a local bump centered at 0″37 in the difference images, with a peak that is $\sim 20\%$ of the full-wedge intensity at that radius.

For the F1280W image, although there is a bright region at the location of the CS, it has roughly the same intensity as, and thus cannot be distinguished from, the nebular spur "spur(nw)" (marked by a magenta ellipse in the F1280W image in Figure 2). For the F1500W, F1800W, and F2550W images, no compact source can be seen at the location of the CS. For these
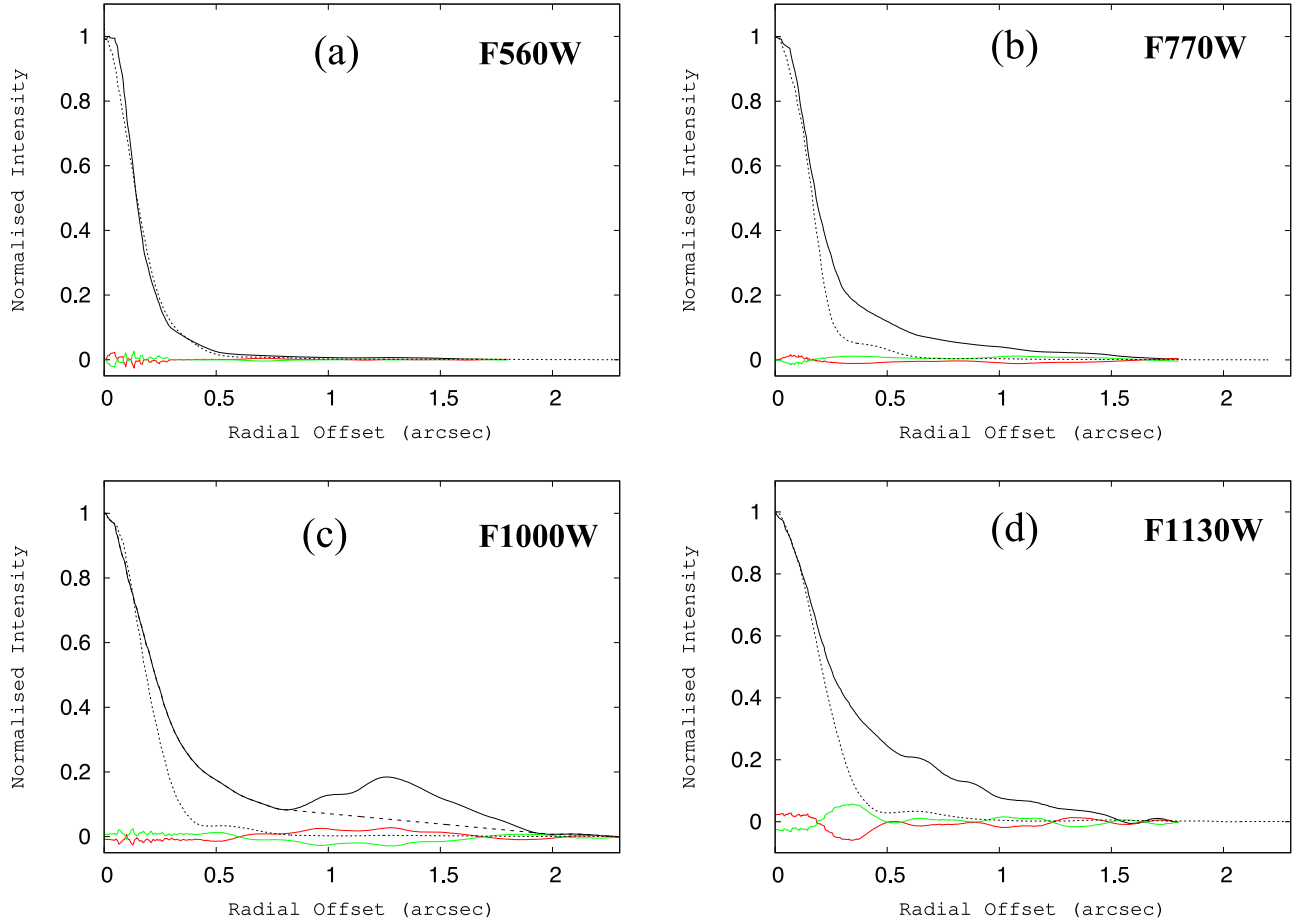
Figure 3. Radial intensity distributions extracted from MIRI images in four different filters (solid black curves), by averaging the intensity over an angular wedge (full-wedge intensity) with its vertex centered on the CS, with the specific angular range chosen to avoid the nebular contamination in the vicinity in each image. Each intensity distribution has been normalized by the corresponding peak intensity, which is 7.44, 4.15, 3.06, and 1.8 MJy sr^{-1}, respectively, for the F560W, F770W, F1000W, and F1130W filters. For each filter, the dotted curves show the PSF extracted from a field star within the field of view, and the red and green curves show the differences between the full-wedge intensity and two half-wedge intensities (see the text for the definition of the "half-wedge intensity"). The broad bump in the F1000W radial intensity at a radial offset of about 1″25 is due to a faint nebular structure in the F1000W image that cuts across the angular wedge used for extracting the radial intensity; the dashed line shows a linear interpolation of the intensity across the edges of this bump.

filters (i.e., F1280W–F2550W), we determined upper limits to the fluxes as follows: (i) for each image, we estimated the 1σ noise in a circular aperture centered at the location of the CS, with a diameter equal to the FWHM of the PSF in each filter (as determined from field stars); and (ii) assuming that a detectable CS source would have a Gaussian shape with the PSF FWHM and a half-power intensity of 3σ in order to be detectable, we computed the flux of this source and set it to the upper limit on F_{core}. The errors on the fluxes are conservative and mostly arise from the uncertainties in the sky background. We also extracted photometry from the images for filters F560W–F1280W from a circular patch in the near vicinity of the CS (Table 3). The colors of this patch are very different from those of the CS.

3. Stellar Effective Temperature and Luminosity

The published values for the effective temperature of the CSPN vary over the range $T_{eff} \sim (101-162)$ kK (e.g., M. A. Guerrero & O. De Marco 2013; J. B. Kaler & G. H. Jacoby 1989)—the exact value adopted affects the estimated bolometric flux and thus the luminosity of the central star. We have adopted an average value of 135 kK for the WD's effective temperature, T_{eff}, in order to fit a model WD

Table 3
Photometry of Circular Patch Near the CS of NGC 6720

Filter	Flux (mJy)
F560W	0.0039
F770W	0.0026
F1000W	0.028
F1130W	0.003

spectrum to the SED of the CS in the UV–optical wavelength range (Figure 4), as follows.

We computed the stellar spectrum using the Tübingen NLTE Model Atmosphere Package (T. Rauch & J. L. Deetjen 2003; K. Werner et al. 2003, 2012) for $T_{eff} = 135{,}000$ K, using solar abundances and $\log g$ (cm s^{-2}) $= 8$. We note that: (i) an H-only WD model produces a poorer fit for the fluxes at 3 and 3.35 μm, with the model values being significantly higher than the observed fluxes; and (ii) within the wavelength range over which the data are available, the WD models are not sensitive to the exact $\log g$ value. The interstellar extinction toward NGC 6720 has been estimated to be $A_V = 0.27^{mag}$, based on the value of $c(H\beta) = 0.13 \pm 0.04$ by C. R. O'Dell et al. (2009).
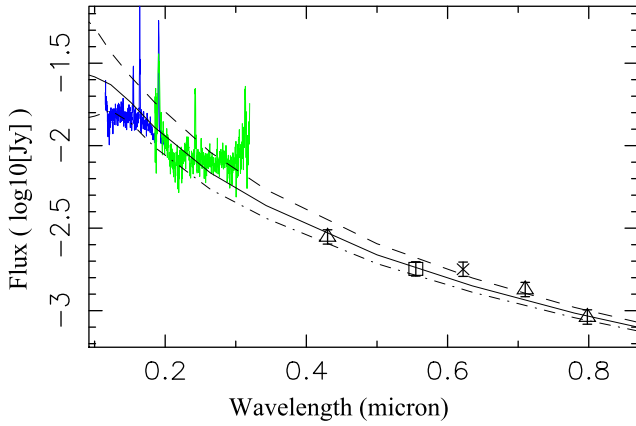
Figure 4. Observed UV spectra and optical photometry (black symbols) of the CS of NGC 6720, together with model SEDs. The model SEDs are of a WD with $T_{eff} = 135,000$ K, $\log g$ (cm s^{-2}) = 8, and luminosity $L = 310\,L_{\odot}$, with three different values of the foreground extinction: $A_V = 0.15^{mag}$ (solid curve), $A_V = 0.0$ (dashed), and $A_V = 0.27^{mag}$ (dashed–dotted). The UV spectra are taken from the IUE MAST archive (data IDs SWP 07230—blue curve and LWR 06238—green curve). The error bars on the observed photometry are conservative estimates.

However, with $A_V = 0.27^{mag}$, the model SED that fits the observed optical photometry is significantly below the observed IUE spectrum in the UV region (Figure 4). We find that $A_V = 0.15^{mag}$ produces a much better fit (Figure 4) to the FUV—we have adopted this value, the resulting bolometric flux, $F_{bol} = 1.6 \times 10^{-8}$ erg cm^{-2} s^{-1}, and the luminosity, $L = 310\,L_{\odot}$, for a distance $D = 790$ pc based on its trigonometric parallax.[22] We find that the observed SED shows an increasing excess over the observed flux at wavelengths greater than ~5 μm. The most likely explanation for this excess is that it arises from the presence of warm/hot dust around the CSPN.

4. Radiative Transfer Modeling of SED and Extended Emission of the CS

We have used the DUSTY and CLOUDY radiative transfer codes (G. J. Ferland et al. 2017; Z. Ivezić et al. 2020) to model the SED, as well as the radial intensity distributions at 5.6, 7.7, 10, and 11.3 μm of the CS. We need both these codes, because (as we show below) we need both thermally and stochastically heated (i.e., PAHs) dust grains, but the DUSTY code can only model emission from dust grains in thermal equilibrium—the CLOUDY code is needed to model the emission from stochastically heated dust grains. Although it is likely that the dust cloud is disk-like, since we have no direct information about its morphology, we have chosen to use 1D modeling. This does not affect our results, because (as we show below) the optical depth of this cloud is $\ll 1$, even at relatively short wavelengths. Even if the dust cloud had a disk configuration, the radial optical depth near and in the equatorial plane would remain well below unity. Although in principle, one should use band-averaged model flux densities for comparison with the observed photometry, we find that the former are not significantly different from the monochromatic flux densities in wavelength regions where the model spectrum shows a monotonic smooth variation, i.e., for $\lambda \lesssim 4\,\mu$m. However, the model spectra (discussed below) do show strong, nonmonotonic variations in the wavelength regions covered by the

bandpasses of the four MIRI filters: F560W, F700W, F1000W, and F1130W filters—hence, for these, we have used band-averaged model flux densities for comparison with the observations. The input parameters and output properties for our best-fit models are given in Table 4.

4.1. Thermal Emission: DUSTY

We first use DUSTY modeling in order to explore the relevant input parameter space, because it provides both the SED as well as the radial intensity distributions directly as part of its output. The main input parameters of the DUSTY model are: (i) the dust temperature at the inner shell radius (T_d); (ii) the total radial optical depth at 0.55 μm (τ_V); (iii) the shell density distribution; (iv) the grain size distribution for a choice of grain composition; (v) the relative shell thickness (Y = the ratio of the shell's outer radius, R_{ou}, to its inner radius, R_{in}); and (vi) the spectrum of the central star—for this, we use the stellar spectrum that was used to fit the UV–optical–near-IR data, as described in Section 3.

The shell density distribution was assumed to be a power law, $\rho_d(r) \propto r^{-p}$. For the grain sizes, we used grains with a fixed radius, a, because we found that we had to vary the grain radius in order to find the best fit. Using, for example, a distribution function for the grain radius, such as the Mathis, Rumpl, and Nordsieck (MRN) one, with $n(a) \propto a^{-q}$ for $a_{min} \leqslant a \leqslant a_{max}$ (J. S. Mathis et al. 1977), would require adjusting the values of three different parameters, which would be significantly more poorly constrained, given our fairly limited observational constraints.

Our best-fitting model (Figure 5) requires silicate grains in order to fit the shape of the SED in the 5–11.3 μm region, specifically the local peak at ~10 μm. Amorphous carbon grains produce a monotonically varying smooth shape that does not fit these data. The dust temperature at the inner shell radius needs to be relatively high, $T_d \gtrsim 1200$ K, in order to produce a bright core with a width that does not exceed the observed one as seen in the radial intensity distributions; the corresponding value of the inner shell radius is 10.5 au. The dust density power-law exponent, p, is constrained by the extended emission in the radial intensity distributions; we find that $p \sim -0.8$ (i.e., with density increasing outward with radius) is needed to fit the extended emission seen in the radial intensity distributions for F1000W and F1130W. We also require the grains to be relatively small, with $a_{max} \lesssim 0.01\,\mu$m, in order for these to be warm enough in the extended parts of the dust cloud to produce adequate emission there—using larger grains results in grain temperatures too low to produce the extended emission. The outer radius of the shell, corresponding to our best-fit model value of $Y = 125$, is ~1300 au.

However, this model shows a significant lack of extended emission for F770W, and the total model flux at 7.7 μm is much less than observed. The model also has inadequate emission to fit the F560W photometry well, although the discrepancy is much less than for F770W. We investigated models with mixtures of silicate and amorphous carbon grains, but the resulting best-fit model was worse than the silicate-only model—specifically, the model radial intensities in the F1130W and F1000W filters provide a significantly worse fit (Figure 6), compared to the silicate-only model. We show in the next section (Section 4.2) a path forward to help resolve these discrepancies, by adding very small grains that can be heated stochastically to much higher temperatures than are possible for larger grains in thermal equilibrium.

---

[22] From Gaia DR3 (Gaia Collaboration 2023)—see R. Wesson et al. (2024).

Table 4
Best-fit Models of the Dust Emission Toward the CS of NGC 6720

T_d(in)[a] (K)	R_{in}[b] (arcsec, au)	T_d(out) (K)	R_{out}[c] (arcsec, au)	n[d]	τ_V[e]	F_{bol} (erg s^{-1} cm^{-2})	Dust Comp.	M_d[f] ($M_\oplus$)
1500	0″013, 10.5	151	1″66, 1310	−0.8	1.3×10^{-8}	1.6×10^{-6}	Silicate	1.86×10^{-6}
1688	...	238	...	...	...	...	PAH	7.27×10^{-7}

Notes.
[a] The (input/output) dust temperature at the shell inner radius for silicate/PAH dust.
[b] The (output) dust temperature at the shell outer radius.
[b] The (inferred) inner radius of the dust shell.
[c] The (input) outer radius of the dust shell.
[d] The (input) exponent of the density power law ($\rho_d(r) \propto r^{-n}$) in the dust shell.
[e] The (input) dust shell's optical depth at 0.55 μm.
[f] The (inferred) circumstellar dust mass.

There are additional small discrepancies between the observed and model fluxes at 10 and 11.3 μm—the model flux at 10 μm (11.3 μm) is slightly below (above) the observed lower (upper) limits on the observed fluxes. A plausible explanation for these discrepancies is that the intrinsic shape of the 10 μm emission feature in the CS is different from the assumed model one; this explanation is supported by the varied shapes of this feature, as observed in the dust emission from a sample of WDs (J. Farihi et al. 2025). JWST/MIRI spectroscopy of the very central regions is needed in order to accurately characterize the shape of the SED and make further progress in understanding the dust cloud around the central star of NGC 6720.

We find the mass of the dust shell (since DUSTY does not provide a direct measure of the shell dust mass) using Equation (1) of R. Sahai et al. (2023), i.e.:

$$M_d = 4\pi \left[(n-1)/(3-n)\right] y(Y) R_{in}^2 (\tau_{10}/\kappa_{10}), \qquad (1)$$

where $y(Y) = (Y^{3-n} - 1)/(1 - Y^{1-n})$ and τ_{10} and κ_{10} are, respectively, the optical depth and the dust mass absorption coefficient at 10 μm. For our best-fit model, $\tau_V = 1.3 \times 10^{-8}$ and $\tau_{10} = 8.3 \times 10^{-9}$. We estimate κ_{10} using the dust properties for uncoagulated silicate dust as tabulated by V. Ossenkopf et al. (1992),[23] which provide the values of $\kappa(\lambda)$ for a standard MRN distribution. Since the grains in our model have a radius $a = 0.01 \mu$m, which is $\sim$20% larger than the density-weighted grain radius for MRN ($a = 0.0083 \mu$m), and $\kappa \propto a^{-1}$, our adopted value of $\kappa_{10} = 1.72 \times 10^3 \,\mathrm{cm}^2\,\mathrm{g}^{-1}$ is obtained by scaling the tabulated value of $\kappa_{10} = 2.07 \times 10^3 \,\mathrm{cm}^2\,\mathrm{g}^{-1}$ by 0.0083/0.01. We derive a total mass of amorphous silicate dust of $1.86 \times 10^{-6} M_\oplus$.

4.2. Stochastic Emission: CLOUDY

We have used version C23.01 of the CLOUDY code (G. J. Ferland et al. 2017) to investigate whether the presence of PAHs in the dust cloud can help resolve the discrepancy between the data and our models at 7.7 μm. Using a dust shell with the same inner and outer radii, and density law, as derived from the DUSTY model, but with a dust composition consisting of charged PAH clusters with 120 atoms,[24] we derive the SED of the emission from these grains (Figure 7, dotted curve) and add it to the SED derived from the DUSTY model (Figure 7, dashed curve). We find a very good fit to the

observed 7.7 μm flux (Figure 7, solid curve). In addition, the relatively smaller discrepancy that we found between the observed and DUSTY model, 5.6 μm flux, is now significantly reduced. The CLOUDY model's 7.7 μm radial intensity is significantly higher than that of the DUSTY model at all radii, as expected, due to the contribution of the nonstochastic PAH emission (Figure 8). We do not attempt to further fine-tune the PAH model, because a very large variety of PAH particles (e.g., with different numbers of C atoms) are likely to be present. We discuss the origin of the PAHs in Section 6 below. The total mass of PAH grains is $7.27 \times 10^{-7} M_\oplus$.

The inclusion of a small amount of gas, e.g., resulting from a tenuous hot stellar wind from the CSPN, with, for example, a density of (say) $\lesssim$0.05 cm^{-3} at the inner radius of the dust shell (see below), produces negligible gaseous line emission, with no significant effect on the model photometry in the broadband filters. The only gaseous line visible is that due to [Ne VI] 7.65 μm; its integrated flux is very small compared to that of the much broader 7.7 μm PAH feature. The model 3.3 μm PAH feature is very weak and contributes negligibly to the flux in the F335M filter. We note that R. Wesson et al. (2024) find evidence for possible weak PAH emission in the F335M and F1000W filters in a narrow ring in the outer parts of the nebular shell, contributing $<$14% and $<$7% to the flux seen in these filters.

4.3. Gas Emission: CLOUDY

The WD central stars of PNs are known to produce hot, line-driven winds that appear very early after the star leaves the AGB (e.g., for $T_{\rm eff} \lesssim 10$ kK) and fade away on the WD cooling track (i.e., for $T_{\rm eff} \gtrsim 105$ kK; see Figure 1 of J. Krtička et al. 2020). The wind mass-loss rate depends mostly on the stellar luminosity (e.g., J. I. Castor et al. 1975; A. A. C. Sander et al. 2017). Models of such winds by J. Krtička et al. (2020) for a CSPN of mass $0.569 M_\odot$ produce a "knee" in the cooling curve at $T_{\rm eff} \sim 117.8$ kK, where the mass-loss rate has dropped to $2.6 \times 10^{-11} M_\odot$ yr^{-1}, the wind speed is 1830 km s^{-1}, and $L_* = 10^3 L_\odot$. Subsequently, the WD enters a rapidly cooling phase, and the mass-loss rates drop very rapidly. For example, the CSPN mass-loss rate is $5.1 \times 10^{-13} M_\odot$ yr^{-1} for $T_{\rm eff} \sim 105.7$ kK, and there is no wind as the WD cools further. In the case of NGC 6720, the current (progenitor) mass is inferred to be 0.58 (1.5–2) $M_\odot$. The CSPN is believed to have reached a peak temperature (i.e., at the knee of the cooling curve) at $L_* = 3 \times 10^3 L_\odot$ (R. Wesson et al. 2024)—thus, given its current luminosity, it is now in the rapidly cooling phase

_____
[23] hera.ph1.uni-koeln.de/~ossk/Jena/tables/mrn0
[24] Using the opacity file ph3c_c120.opc in the CLOUDY C23.01 package.
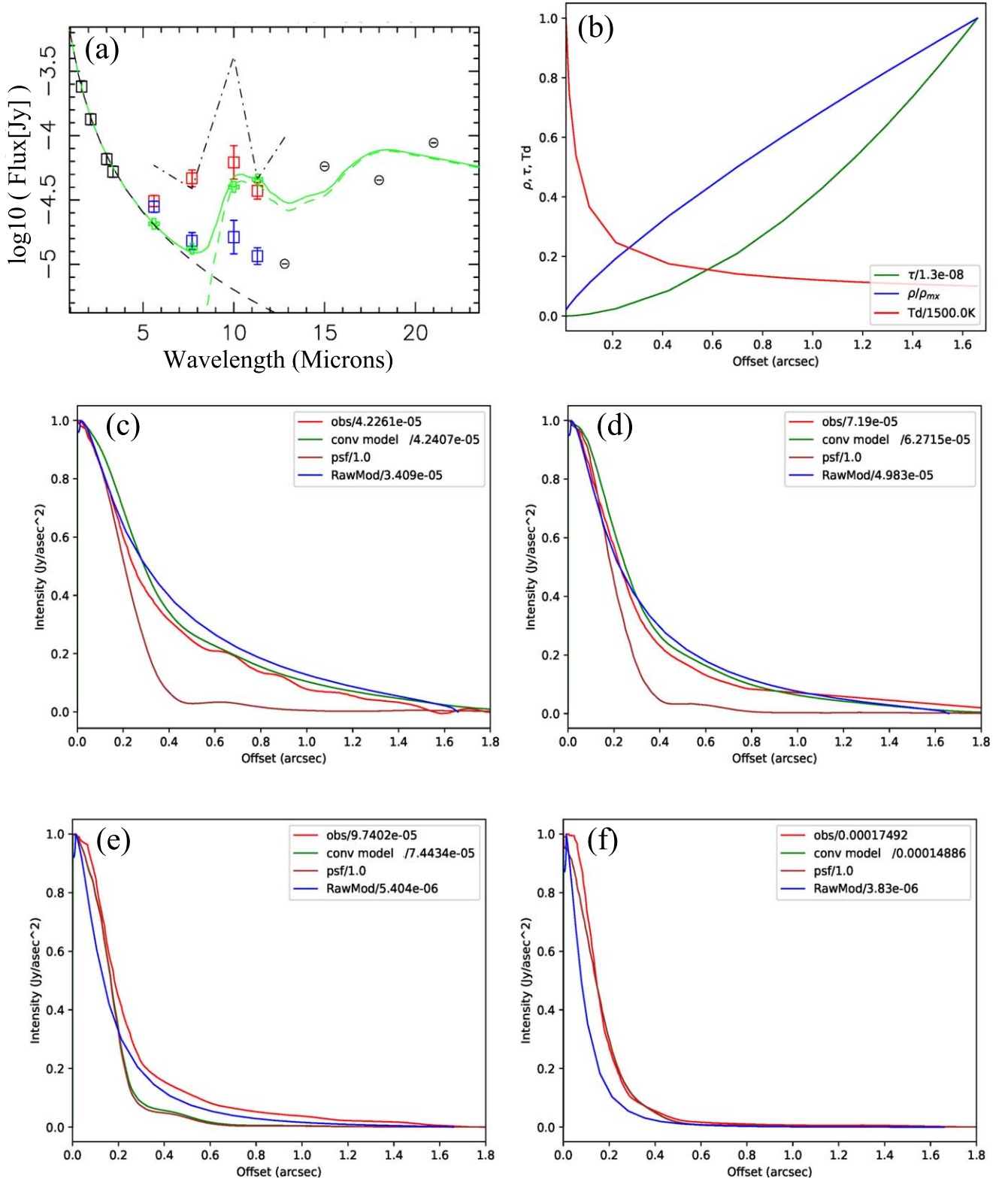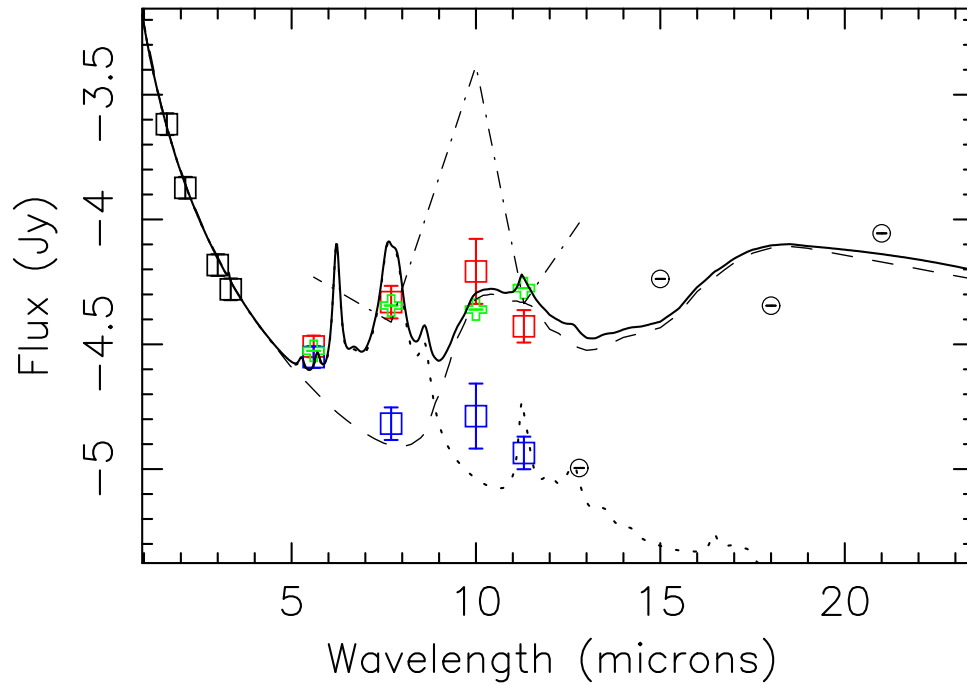
Figure 5. (a) Observed mid-IR photometry (black symbols) and model SED (smooth green curve) for the CS of NGC 6720 and a circumstellar dust shell with silicate grains, with a dust temperature at the inner radius of the shell $T_d = 1500$ K, a density power law $\rho(r) \propto r^{0.8}$, an outer-to-inner radius ratio $Y = 125$, and a dust grain radius 0.01 μm. For $\lambda < 5$ μm, the black boxes show the total flux. For $\lambda > 5$ μm, the red (blue) boxes show the total (core) flux. The circles show the upper limits for the core flux. The error bars on the observed photometry are conservative estimates. The dashed green curve shows the thermal emission from the dust, and the dashed black curve shows the attenuated starlight. The dashed–dotted curve shows the relative fluxes of a patch covering a region of nebular emission in the near vicinity of the CS. The green square symbols show the band-averaged total model fluxes for specific filters. (b) Normalized density, tangential optical depth, and temperature of the dust. The remaining panels show the normalized observed and model (monochromatic, at the center wavelength of each filter) radial intensity distributions of the dust shell for the (c) F1130W, (d) F1000W, (e) F770W, and (f) F560W filters. The numerical division factors in the legends of panels (b)–(f) show the values used for normalization.
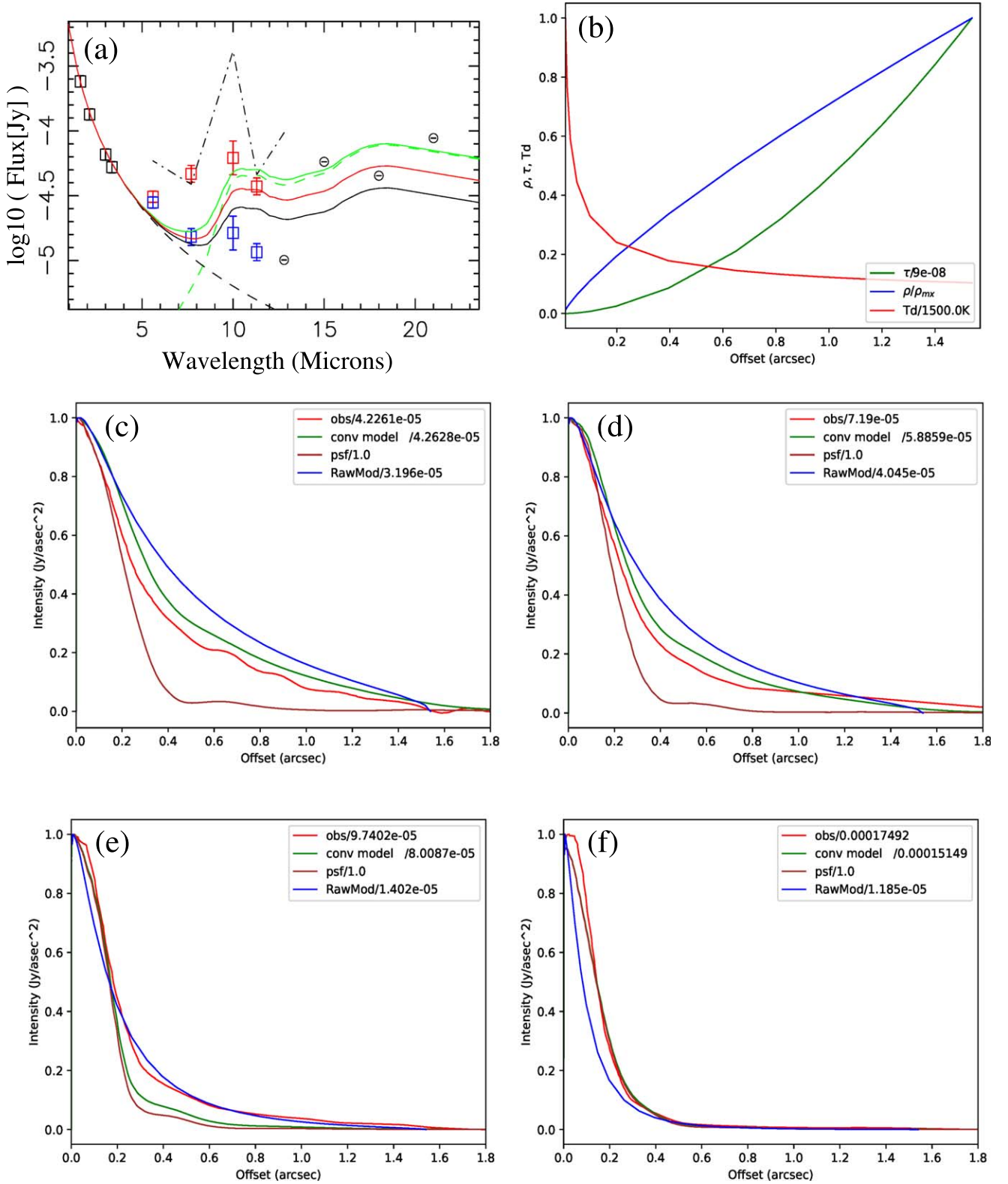
Figure 6. The same as Figure 5 but with a dust composition that is 50% silicate and 50% amorphous carbon.

(R. Wesson et al. 2024). Hence, it appears likely then that the wind mass-loss rate for NGC 6720's CSPN is $\lesssim 10^{-13} M_\odot$ yr^{-1}. The gas density due to such a wind (assuming a typical expansion velocity of 2000 km s^{-1}) at the inner radius of the dust shell, 11.7 au, is $\lesssim 0.05$ cm^{-3}; the resulting line emission is insignificant compared to the dust emission.

4.4. Possible Unresolved Companion

We can constrain the mass of any unseen (unresolved) stellar companion, e.g., such as CSPN(C), from the SED of the CS over the wavelength range where dust emission does not contribute significantly (i.e., $< 5 \mu$m). We have investigated the effect of including the theoretical spectrum of such a

Figure 7. Observed mid-IR photometry (black symbols) and model SED (smooth curve) for the CSPN of NGC 6720 and a circumstellar dust shell with small silicate grains and PAHs. For $\lambda < 5~\mu$m, the black boxes show the total flux. For $\lambda > 5~\mu$m, the red (blue) boxes show the total (core) flux. The dotted curve shows the SED of the PAH emission, and the dashed curve shows the SED of the small silicate grains (+ the central star). The circles show upper limits for the core flux. The error bars on the observed photometry are conservative estimates. The dashed–dotted curve shows the relative fluxes of a patch covering a region of nebular emission in the near vicinity of the CS. The green square symbols show the band-averaged model fluxes.
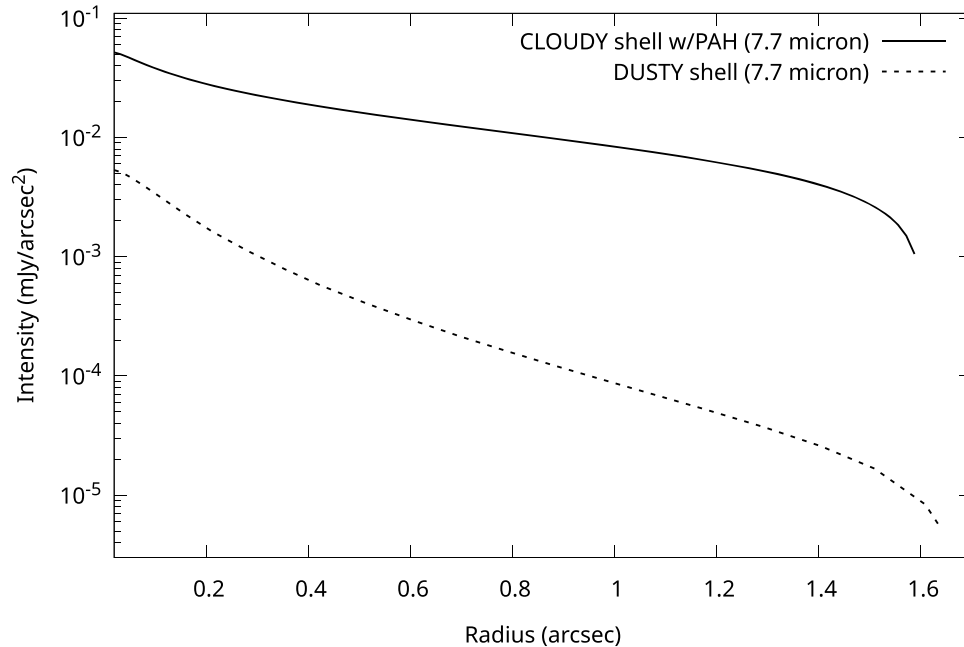
Figure 8. The 7.7 μm radial intensity from the best-fit CLOUDY model (small silicate grains and PAHs) compared to that from the best-fit DUSTY model (small silicate grains only).

companion with a range of spectral types of M7.5V or later, since for an M7.5V companion, the resulting flux at 3.35 μm is 20% more than that observed—well above the observed upper limit. The values of luminosity and effective temperature for late-type MS dwarfs have been taken from C. Cifuentes et al. (2020). The model spectra have been extracted from the BT-NextGen (AGSS2009) data set[25] (F. Allard et al. 2012). The

results of this modeling (Table 5) show that the highest-mass unresolved MS companion that can be present and remain undetected is less massive than an M dwarf with spectral type M9.5V, with $L \sim 2.35 \times 10^{-4} L_\odot$ and $T_{\rm eff} \sim 2300$ K. An M9.5V companion increases the model SED flux in the F356M filter by 13%, above the upper limit on the observed F335M flux. Noting that the model luminosities are also uncertain, we find that if we peg the M7.5V and M8.0V models at their lower-limit luminosities, the resulting F356M model
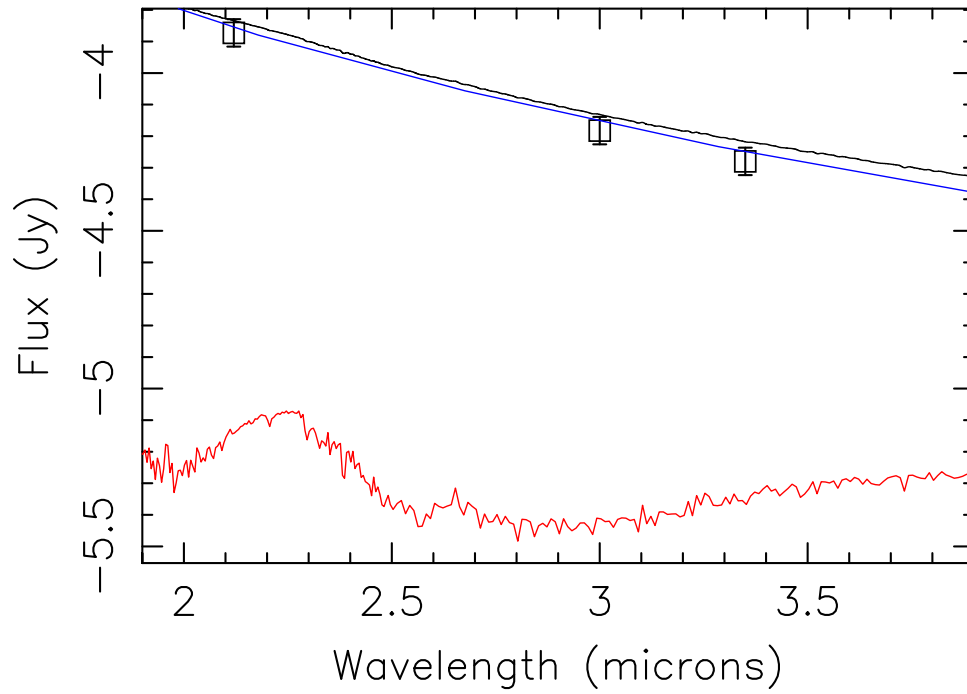
Figure 9. Model SED of the CSPN (blue curve), an M8 MS companion (red curve), and the total SED (CSPN + M8; black curve), together with the observed photometry (black rectangles).

Table 5
Effect of an MS Stellar Companion on the SED of the CS of NGC 6720

Spectral[a] Type	$T_{\rm eff}$[a] (K)	Luminosity[a] ($10^{-4} L_\odot$)	Mass[a] ($M_\odot$)	$F_{\rm mod}(3.35\ \mu{\rm m})/F_{\rm obs}\ (3.35\ \mu{\rm m})$
M7.5V	2500 ± 82	5.8 ± 1.2	0.104 ± 0.009	1.20
M8.0V	2500 ± 91	5.1 ± 1.6	0.104 ± 0.014	1.19
M9.5V	2300 ± 45	2.69 ± 0.35	0.077 ± 0.008	1.13
L0.5V	2200 ± 61	2.17 ± 0.15	0.079 ± 0.004	1.13
L1.5V	2000 ± 172	1.81 ± 0.35	0.094 ± 0.016	1.12

Note.
[a] From C. Cifuentes et al. (2020).

flux values are still 18% and 15% above the observed values. We conservatively conclude that a companion, if present, is of spectral type M8.0 or later, implying a mass $\leqslant 0.1\ M_\odot$. Figure 9 shows model SEDs of an M8 MS companion and the total SED (CSPN + M8), together with the observed photometry in the wavelength range that is most sensitive to low-mass companions.

5. CS Photometric Variability

For the CS of NGC 6720, the value of the Gaia variability flag, "phot_variable_flag," is VARIABLE. Light curves for it are available in the Gaia photometric bands G, Bp, and Rp.[26] We have downloaded and analyzed these light curves, which cover a period of ∼950 days. We first examined the G-band data, as these have the highest signal-to-noise ratio (S/N). The cadence is such that there are multiple pairs of successive data points that are very close in time (<0.2 days; "close-time-clustered" data points), compared to the median time interval ($\gtrsim$30 days). In addition, there was one point for which the

fractional flux error was much larger than the median fractional flux error, i.e., by $6.5\sigma_{\rm err}$, where $\sigma_{\rm err}$ is the standard deviation of the fractional flux errors. We rejected this point, reducing $\sigma_{\rm err}$ by a factor of 2.6 in the resulting data set (with 49 data points in total). We then removed two outliers with flux values outside $\pm 3\sigma$ of the error-weighted mean flux, $F(G)_{\rm ave} = 10397\ {\rm e^-\ s^{-1}}$, further reducing the error-weighted standard deviation in the flux, $\sigma_{F(G)}$, from 108 to 85 (Figure 10, top panel, cyan symbols). The fluxes of the close-time-clustered data points (Figure 10, bottom panel) were averaged to produce a final data set of 28 data points (with $\sigma_{F(G)} = 82$; Figure 10, top panel, red symbols). The statistics of the various data sets are summarized in Table 6—the value of $F(G)_{\rm ave}$ does not change significantly across these data sets.

The flux variations of the CS are relatively small—for the outliers-removed data set, we find $\sigma_{F(G)}/F(G)_{\rm ave} = 0.0082$. We therefore first consider whether scan-angle-dependency of the Gaia epoch photometry (B. Holl et al. 2023a) could be responsible for producing spurious variability in the G band. B. Holl et al. (2023a) provide two important parameters for assessing whether the G-band photometric variability results from scan-angle-dependency, labeled spearmanCorrIPDgFoV

---

[26] Gaia DR3 Part 1. Main source: I/355—https://cdsarc.cds.unistra.fr/viz-bin/cat/I/355 (Gaia Collaboration 2023).

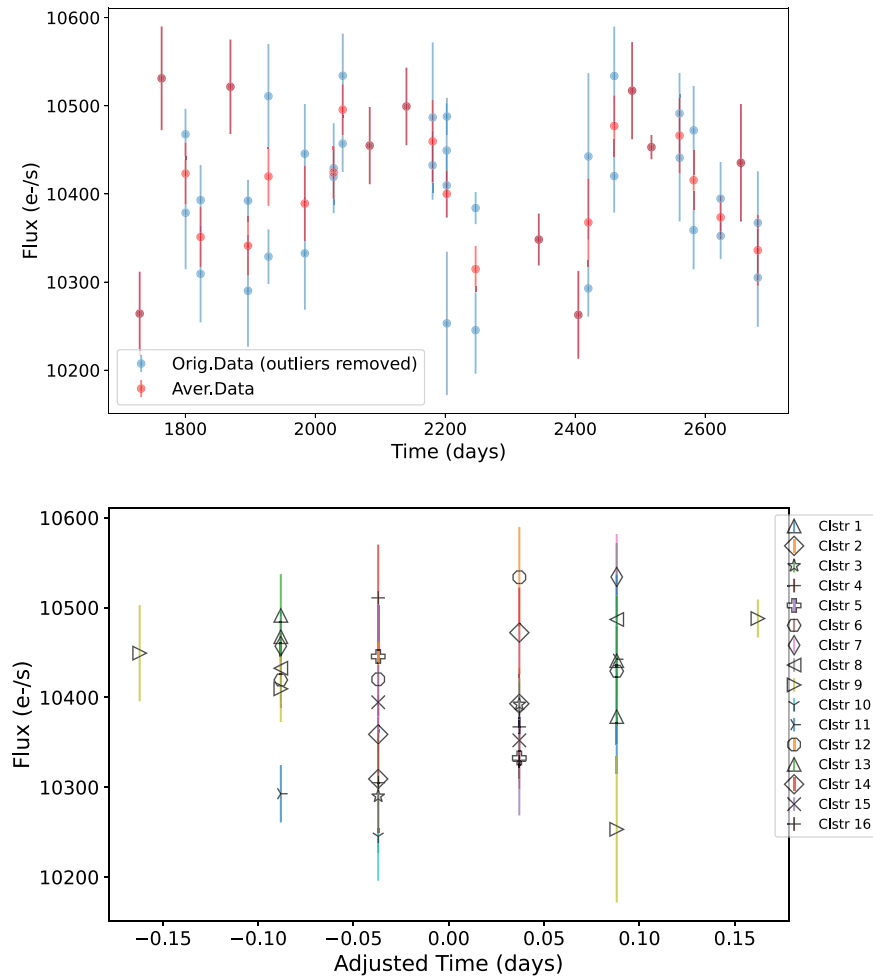**Figure 10.** (Top) Gaia DR3 *G*-band count rate as a function of time for the CS of NGC 6720: original data with one bad data point and two 3σ outliers removed (cyan symbols) and with close-time-clustered points averaged (red symbols). (Bottom) The *G*-band count rates for the close-time-clustered data points, with the mean time for each cluster set to 0.

(also r_{ipd}) and spearmanCorrExfgFoV (also r_{exf}) in their variability catalog—doi:10.26093/cds/vizier.36740025 (B. Holl et al. 2023b). Relatively high absolute values of these parameters,[27] i.e., $|r_{\mathrm{ipd}}|$ and $|r_{\mathrm{exf}}|$, indicate that the variability is spurious, and several studies that have extracted astrophysically variable sources using the *G*-band photometry (e.g., M. I. Carnerero et al. 2023; E. Distefano et al. 2023; T. Lebzelter et al. 2023; N. Mowlavi et al. 2023) have rejected sources for which $|r_{\mathrm{ipd}}| > 0.7$ and $|r_{\mathrm{exf}}| > 0.7$. However, since the values of these parameters for the CS of NGC 6720 are very small ($r_{\mathrm{ipd}} = 0.12$ and $r_{\mathrm{exf}} = -0.16$), we conclude that its observed flux variability is real.

The final data set was subjected to Lomb–Scargle periodogram analysis, revealing a strong peak corresponding to a period of $P = 383$ days, with an amplitude and phase of, respectively, 66.4 e$^-$ s^{-1} (0.64% of the median flux) and 0.20, and a false-alarm probability FAP $= 0.2$.[28] We then made a sinusoidal fit of the model to the data, then a few data points that were found to be offset by more than 3σ from the fitted curve (a total of three) were removed from the data set, and a second Lomb–Scargle periodogram analysis was carried out.

<hr/>

[27] The range is 0–1.
[28] The probability of observing the peak in a random, noise-only time series (i.e., a lower FAP value indicates that the peak is more significant).

Table 6
Gaia *G*-band Time Series of the CS of NGC 6720: Statistics

Data Set Descr.	No. of Data Points	Wtd. Mean (e$^-$ s^{-1})	Std. Dev (e$^-$ s^{-1})
Original	50	...	...
Bad data removed	49	10,397	107.6
Outliers removed	47	10,401	85.1
CloseDataPts averaged	28	10,398	81.6

This resulted in a slightly stronger peak at $P = 371$ days (Figure 11), with an amplitude and phase, respectively, of 59.7 e$^-$ s^{-1} (0.57% of the median flux) and the same FAP.

An FAP value <0.05 is generally considered statistically significant, whereas an FAP value > 0.1 indicates a less significant peak, likely due to noise. The FAP value is calculated based on the assumption that the time series is noise-only; if there are other sources of variability in the data, the FAP may not be accurate.

The light curves in the Bp and Rp filters (Figures 12) are of lower S/N than in the *G*-band filter and do not show an obvious periodicity.

In order to investigate whether the possible periodicity that we observe in the *G*-band-filter light curve is an instrumental artifact, we have inspected the light curves of six field stars
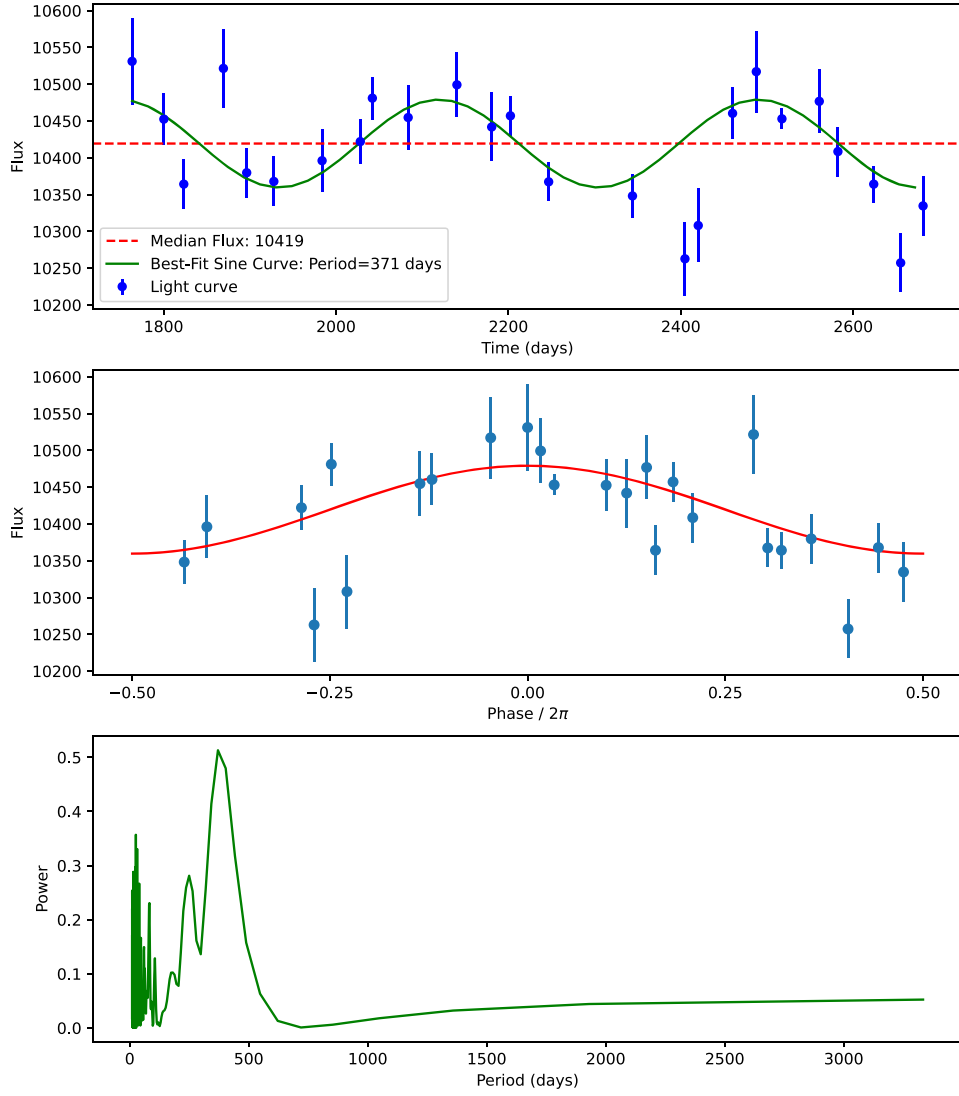
Figure 11. (Top) Gaia DR3 G-band light curve of the CS of NGC 6720, overlaid with the best-fitting sinusoidal model, with period $P = 371$ days. (Middle) Phase-folded Gaia DR3 G-band light curve of the CS of NGC 6720, overlaid with the best-fitting sinusoidal model. (Bottom) Lomb–Scargle periodogram of the light curve in the top panel.

Table 7
Field Stars with G-band Light Curves Near the CS of NGC 6720

Name	Offset (arcsec)	R.A. (J2000) (hh mm ss)	Decl. (J2000) (dd mm ss)	Gmag[a] (mag)	phot_variable_flag	$r_{ipd,G}$[b]	$r_{exf,G}$[c]
FS1	103.578	18 53 31.9920361623	+33 03 21.015084474	16.416496	VARIABLE	−0.030698	−0.278665
FS2	179.898	18 53 45.9813883771	+33 03 41.753314212	16.401575	VARIABLE	−0.074560	−0.189189
FS3	213.640	18 53 32.9190411134	+32 58 13.093566670	15.875365	VARIABLE	−0.173693	0.189916
FS4	245.875	18 53 21.6164058659	+33 04 43.133991427	14.591276	VARIABLE	0.184214	0.112892
FS5	271.235	18 53 16.7110519429	+33 04 07.034403143	13.829674	VARIABLE	−0.056917	−0.150474
FS6	274.113	18 53 35.1056734346	+32 57 11.036167760	13.910662	VARIABLE	−0.045757	−0.047561

Notes.
[a] Gaia DR3 G-band mean magnitude.
[b] spearmanCorrIPDgFoV from table J/A+A/674/A25/vspursig.
[c] spearmanCorrExfgFoV from table J/A+A/674/A25/vspursig.

within a $5'$ radius of the CS that have similar G-band magnitudes or are slightly brighter (Table 7). The field stars show similar or lower variability amplitudes (Figure 13); these flux variations are real, because the values of r_{ipd} and r_{exf} for these sources are relatively small. We have carried out Lomb–Scargle periodogram analysis on these and we find that none of them show evidence for significant periodicity. We conclude that the G-band periodicity that we find for the CS of NGC 6720, if significant, is most likely of astrophysical origin and not an artifact.
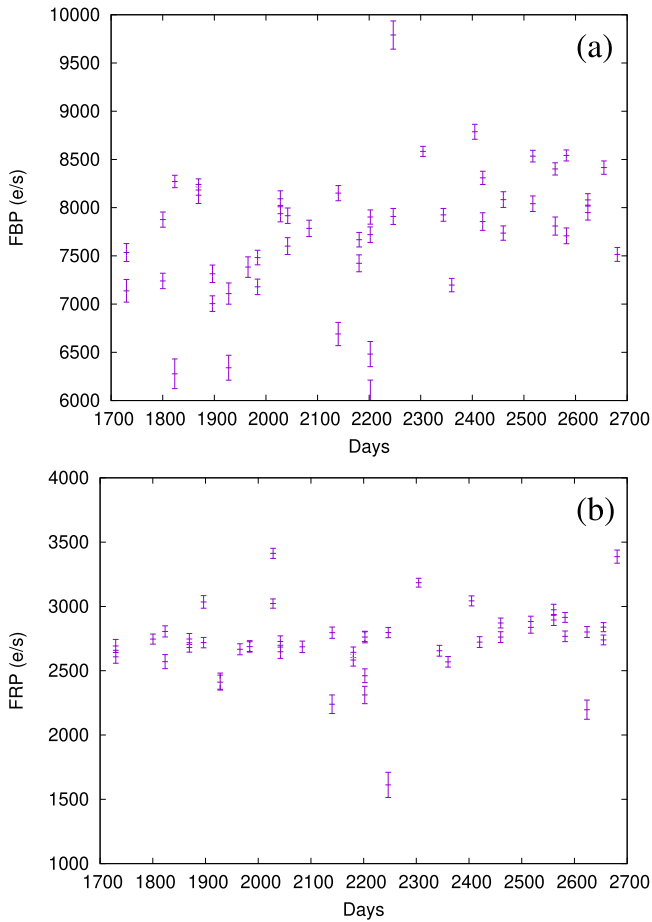
Figure 12. Light curves of the CS of NGC 6720 in the (a) Gaia DR3 BP-filter and (b) Gaia DR3 RP-filter.

The very short-term time variations of the G-band flux, as shown by the scatter of the fluxes in close-time-clustered points, are comparable to the longer-term variations, suggesting that either the CS: (i) has only short-term variations, and the (low-significance) 383 days period is not real; or (ii) has both a short-term variation and a longer-term variation that is periodic, resulting in a relatively high FAP for the latter in the Lomb–Scargle analysis.

The mass of any close companion that could be responsible for the variability must be $\leqslant 0.1\,M_\odot$, based on our modeling of the SED (Section 4.4). Assuming that the 371 days periodicity is real and due to the orbital motion of the companion, the latter would (on average) be separated by 0.9 au from the CSPN.

6. Discussion

If the dust cloud around the CSPN includes the presence of PAHs, as we have proposed above, these will require continuous replenishment. This is because the strong UV radiation field of the CSPN is likely to photodissociate PAHs (which are generally small, $\lesssim 5$–10 Å) very quickly. Given a typical dissociation energy of a bond within a PAH of ~ 5 eV, and a photon rate of $\sim 2 \times 10^{46}\,\mathrm{ph\,s^{-1}}$, a 50 carbon PAH, taking a far-UV absorption cross section of $3.5 \times 10^{-16}\,\mathrm{cm^2}$ (A. G. G. M. Tielens 2008), will be fully destroyed in about 1.5 hr at a typical radius of 600 au, in the extended part of the dust cloud around the CSPN.

The replenishment can occur via the outgassing of cometary bodies and/or the collisional grinding of planetesimals (J. Y. Seok & A. Li 2015, 2017). In addition to outgassing, UV irradiation can generate dust particles that are larger than PAHs but that can also emit the broad features generally labeled aromatic IR bands (S. Kwok et al. 2001; S. Kwok 2022)—these include a very strong, broad feature at $\sim 8\,\mu$m. Such dust grains consist of mixed aromatic/aliphatic organic nanoparticles (MAONs), a carbonaceous compound containing aromatic rings of different sizes and aliphatic chains of different lengths and orientations arranged in a 3D amorphous structure. S. Kwok et al. (2001) suggest that UV irradiation continuously transforms aliphatic to aromatic groups in MAONs.

Such outgassing and/or collisional grinding of planetesimals, left over from the MS phase of the primary, has been proposed as one mechanism for explaining the presence of the compact dust cloud around the CSPN of the PN NGC 3132, resulting from the dynamical evolution of a triple-star system (R. Sahai et al. 2023). As in the case of NGC 3132, it is possible that the three stars CSPN(A), CSPN(B), and CSPN(C) formed a stable hierarchical triple system while all the stars were on the MS (with an inner binary and a more distant tertiary) but became dynamically active on much longer timescales due to the "Eccentric Kozai–Lidov" (EKL) mechanism (Y. Kozai 1962; M. L. Lidov 1962; S. Naoz 2016). It has been shown that the EKL mechanism can cause the inner binary to undergo large-amplitude eccentricity and inclination oscillations, driving it to have very small pericenter distances and even to merge (e.g., S. Prodan et al. 2015; A. P. Stephan et al. 2018), and cause the tertiary to move out to a large orbit or become unbound.

Alternatively, the dust cloud in the CS of NGC 6720 could have resulted from a strong binary interaction, when the primary was a red giant branch or AGB star, leading to the formation of stable circumbinary disks of gas and dust in Keplerian rotation (e.g., H. Van Winckel 2019; J. Kluska et al. 2022) with total masses (gas + dust) in the range a few $\times\,10^{-3}$–$10^{-2}\,M_\odot$ (e.g., I. Gallardo Cava et al. 2021). In contrast, the total dust mass that we derive for NGC 6720's CS is relatively low ($\sim 2.6 \times 10^{-6}\,M_\oplus$). It is much less than even the masses of the large asteroids in the solar system, e.g., Ceres ($1.57 \times 10^{-4}\,M_\oplus$), Vesta ($4.34 \times 10^{-5}\,M_\oplus$), and Pallas ($4.34 \times 10^{-5}\,M_\oplus$) but larger than those of small asteroids such as Siwa ($2.5 \times 10^{-7}\,M_\oplus$) and much larger than carbonaceous asteroids such as Bennu ($1.31 \times 10^{-14}\,M_\oplus$). In summary, if the dust cloud in NGC 6720's CS is indeed a remnant of the disk resulting from binary interaction during an earlier evolutionary phase of the CSPN, it is clear that such a disk has now been almost completely dissipated.

The presence of a very close companion to CSPN(A) is suggested by the significant photometric variability of the CS (irrespective of whether or not a periodic signal is present; e.g., A. Aller et al. 2020; A. Ali & A. Mindil 2023; M. Gładkowski et al. 2024). Such "extrinsic" variability may arise due to the operation of different mechanisms, such as the irradiation of a cold MS companion by the hot CSPN, ellipsoidal variability, and eclipses. Assuming that the orbital plane of the companion is the same as the equatorial plane of NGC 6720, and the nebula is viewed nearly pole-on, eclipses of the CS by the companion are an unlikely explanation. This very close companion could either be CSPN(C), having moved inward
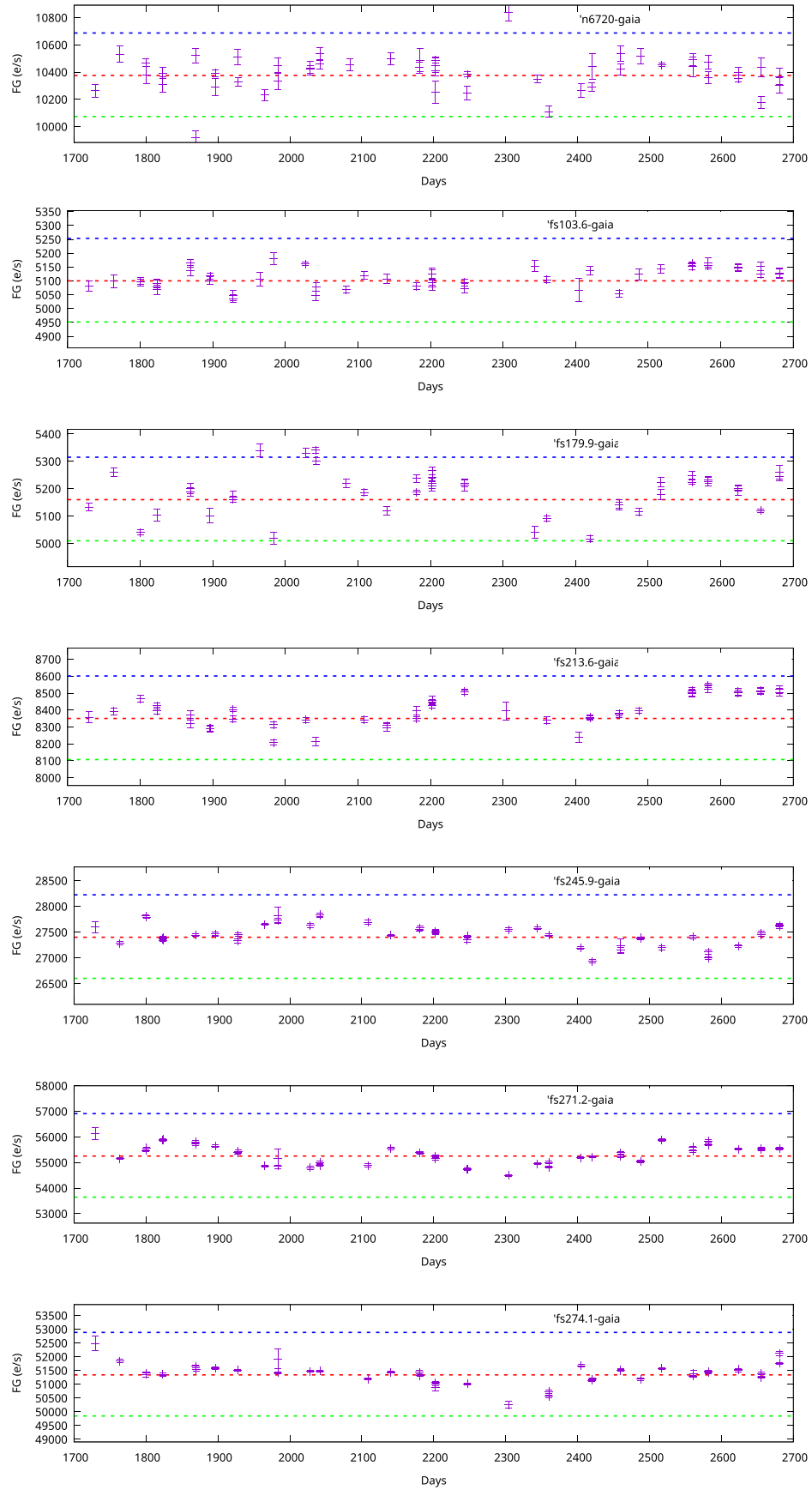
Figure 13. Gaia DR3 *G*-filter light curve of the CS of NGC 6720 compared with that of six field stars. In each panel, the red dashed lines show the mean flux (e s^{-1}), whereas the blue (green) lines shows a flux value that is 3% more (less) than the mean.

15

as a result of the EKL mechanism, or it could be a third companion of CSPN(A). However, the photometric variability of the CS could also be intrinsic to the CSPN, due to nonradial pulsations or spots on the surface of the WD. For example, a recent survey of Gaia DR3, TESS, and Zwicky Transient Facility data revealed flux variations with periodicities from minutes to days (M. Steen et al. 2024) in a sample of 105 WDs that have been attributed to these phenomena.

7. Conclusions

We have used JWST imaging in the near-to-mid-IR wavelength range to investigate the central star of the PN NGC 6720 and its close vicinity. Our main findings are as follows:

1. The central star is surrounded by a compact dust cloud—evidence for this cloud comes from excess emission seen in the SED at wavelengths $\gtrsim 5 \mu m$ as well as radially extended emission in the 7.7, 10, and 11.3 μm images.

2. We have modeled the SED spanning the UV-to-mid-IR wavelength range using the DUSTY radiative transfer code. The UV-to-near-IR wavelength SED shows the presence of a CSPN of luminosity $310\, L_\odot$, with a line-of-sight interstellar extinction of $A_V = 0.15^{\mathrm{mag}}$, assuming a stellar effective temperature of 135 kK, based on published studies. Our best-fit model provides a good fit to the radial intensity distributions of the CS at 10.3 and 11 μm and shows that the dust cloud has a size of ~ 2600 au and consists of relatively small amorphous silicate dust grains (radius $\sim 0.01 \mu m$), with a total mass of $1.9 \times 10^{-6}\, M_\oplus$. However, this model shows a very significant lack of extended emission at 7.7 μm.

3. We find, using the CLOUDY radiative transfer code, that in order to fit the 7.7 μm emission, we require a smaller (but uncertain) mass, $7.3 \times 10^{-7}\, M_\oplus$, of (stochastically heated) ionized PAHs, excited by the UV radiation from the CSPN. Since the same radiation also rapidly destroys PAH molecules, we speculate that these are likely being continuously replenished via the outgassing of cometary bodies and/or the collisional grinding of planetesimals.

4. We find significant photometric variability of the CS that could be due to the presence of a close MS dwarf companion of mass $\leqslant 0.1\, M_\odot$.

ORCID iDs

Raghvendra Sahai https://orcid.org/0000-0002-6858-5063
Peter A. M. van Hoof https://orcid.org/0000-0001-7490-0739
Albert Zijlstra https://orcid.org/0000-0002-3171-5469
Kevin Volk https://orcid.org/0000-0002-3824-8832
Harriet L. Dinerstein https://orcid.org/0000-0002-4017-5572
Michael J. Barlow https://orcid.org/0000-0002-3875-1171
Els Peeters https://orcid.org/0000-0002-2541-1602
Arturo Manchado https://orcid.org/0000-0002-3011-686X
Mikako Matsuura https://orcid.org/0000-0002-5529-5593
Jan Cami https://orcid.org/0000-0002-2666-9234
Nick L. J. Cox https://orcid.org/0000-0002-7926-4492
Isabel Aleman https://orcid.org/0000-0002-7989-9041
Kay Justtanont https://orcid.org/0000-0003-1689-9201
Patrick J. Kavanagh https://orcid.org/0000-0001-6872-2358
Roger Wesson https://orcid.org/0000-0002-4000-4394

References

Ali, A., & Mindil, A. 2023, RAA, 23, 045006
Allard, F., Homeier, D., & Freytag, B. 2011, in ASP Conf. Ser. 448, 16th Cambridge Workshop on Cool Stars, Stellar Systems, and the Sun, ed. C. Johns-Krull, M. K. Browning, & A. A. West (San Francisco, CA: ASP), 91
Aller, A., Lillo-Box, J., Jones, D., et al. 2020, A&A, 635, A128
Balick, B., Gonzalez, G., Frank, A., et al. 1992, ApJ, 392, 582
Ballering, N. P., Levens, C. I., Su, K. Y. L., et al. 2022, ApJ, 939, 108
Bilíková, J., Chu, Y.-H., Gruendl, R. A., et al. 2012, ApJS, 200, 3
Bryce, M., Balick, B., & Meaburn, J. 1994, MNRAS, 266, 721
Carnerero, M. I., Raiteri, C. M., Rimoldini, L., et al. 2023, A&A, 674, A24
Castor, J. I., Abbott, D. C., & Klein, R. I. 1975, ApJ, 195, 157
Chu, Y.-H., Su, K. Y. L., Bilikova, J., et al. 2011, AJ, 142, 75
Cifuentes, C., Caballero, J. A., Cortés-Contreras, M., et al. 2020, A&A, 642, A115
Clark, N., Peeters, E., Cox, N. L. J., et al. 2025, MNRAS, submitted
de Ruyter, S., van Winckel, H., Maas, T., et al. 2006, A&A, 448, 641
De Marco, O., Passy, J.-C., Frew, D. J., Moe, M., & Jacoby, G. H. 2013, MNRAS, 428, 2118
Decin, L. 2021, ARA&A, 59, 337

Distefano, E., Lanzafame, A. C., Brugaletta, E., et al. 2023, A&A, 674, A20
Farihi, J., Su, K. Y. L., Melis, C., et al. 2025, ApJL, 981, L5
Ferland, G. J., Chatzikos, M., Guzmán, F., et al. 2017, RMxAA, 53, 385
Gaia Collaboration 2023, A&A, 674, A1
Gallardo Cava, I., Gómez-Garrido, M., Bujarrabal, V., et al. 2021, A&A, 648, A93
Gładkowski, M., Hajduk, M., Smolec, R., et al. 2024, A&A, 682, A70
Gonzalez-Santamaria, I., Manteiga, M., Manchado, A., et al. 2021, A&A, 656, A51
Guerrero, M. A., & De Marco, O. 2013, A&A, 553, A126
Guerrero, M. A., Manchado, A., & Chu, Y.-H. 1997, ApJ, 487, 328
Hillen, M., Van Winckel, H., Menu, J., et al. 2017, A&A, 599, A41
Holl, B., Fabricius, C., Portell, J., et al. 2023a, A&A, 674, A25
Holl, B., Fabricius, C., Portell, J., et al. 2023b, yCat, 367, 40025
Ivezić, Z., Nenkova, M., Heymann, F., & Elitzur, M. 2020, User Manual for DUSTY, V4, https://github.com/ivezic/dusty/blob/master/release/dusty/docs/manual.pdf
Kaler, J. B., & Jacoby, G. H. 1989, ApJ, 345, 871
Kastner, J. H., Wilner, D., Ryder, D., et al. 2025, ApJ, 981, 46
Kluska, J., Van Winckel, H., Coppée, Q., et al. 2022, A&A, 658, A36
Kozai, Y. 1962, AJ, 67, 591
Krtička, J., Kubát, J., & Krtičková, I. 2020, A&A, 635, A173
Kwok, S. 2022, Ap&SS, 367, 16
Kwok, S., Volk, K., & Bernath, P. 2001, ApJL, 554, L87
Lebzelter, T., Mowlavi, N., Lecoeur-Taibi, I., et al. 2023, A&A, 674, A15
Lidov, M. L. 1962, P&SS, 9, 719
Mathis, J. S., Rumpl, W., & Nordsieck, K. H. 1977, ApJ, 217, 425
Mowlavi, N., Holl, B., Lecoeur-Taïbi, I., et al. 2023, A&A, 674, A16

Naoz, S. 2016, ARA&A, 54, 441
O'Dell, C. R., Ferland, G. J., Henney, W. J., et al. 2013, AJ, 145, 92
O'Dell, C. R., Henney, W. J., & Sabbadin, F. 2009, AJ, 137, 3815
Ossenkopf, V., Henning, T., & Mathis, J. S. 1992, A&A, 261, 567
Prodan, S., Antonini, F., & Perets, H. B. 2015, ApJ, 799, 118
Rauch, T., & Deetjen, J. L. 2003, in ASP Conf. Proc. 288, Stellar Atmosphere Modeling, ed. I. Hubeny et al. (San Francisco, CA: ASP), 103
Rieke, G. H., Su, K. Y. L., Stansberry, J. A., et al. 2005, ApJ, 620, 1010
Sahai, R., Bujarrabal, V., Quintana-Lacaci, G., et al. 2023, ApJ, 943, 110
Sahai, R., Huang, P.-S., Scibelli, S., et al. 2022, ApJ, 929, 59
Sahai, R., Morris, M., Sánchez Contreras, C., et al. 2007, AJ, 134, 2200
Sahai, R., Morris, M. R., & Villar, G. G. 2011, AJ, 141, 134
Sahai, R., Morris, M. R., Werner, M. W., et al. 2012, A&A, 542, L20
Sander, A. A. C., Hamann, W.-R., Todt, H., et al. 2017, A&A, 603, A86
Seok, J. Y., & Li, A. 2015, ApJ, 809, 22
Seok, J. Y., & Li, A. 2017, ApJ, 835, 291
Steen, M., Hermes, J. J., Guidry, J. A., et al. 2024, ApJ, 967, 166
Stephan, A. P., Naoz, S., & Gaudi, B. S. 2018, AJ, 156, 128
Su, K. Y. L., Chu, Y.-H., Rieke, G. H., et al. 2007, ApJL, 657, L41
Tielens, A. G. G. M. 2008, ARA&A, 46, 289
Van Winckel, H. 2019, in The Impact of Binary Stars on Stellar Evolution, ed. G. Beccari & H. M. J. Boffin (Cambridge: Cambridge University Press), 92
Werner, K., Deetjen, J. L., Dreizler, S., et al. 2003, Stellar Atmosphere Modeling, 288, 31
Werner, K., Dreizler, S., & Rauch, T. 2012, TMAP: Tübingen NLTE Model-Atmosphere Package, Astrophysics Source Code Library, ascl:1212.015
Wesson, R., Matsuura, M., Zijlstra, A. A., et al. 2024, MNRAS, 528, 3392
Whitmore, B. C., Allam, S. S., Budavári, T., et al. 2016, AJ, 151, 134